THE PENNSYLVANIA STATE UNIVERSITY
SCHREYER HONORS COLLEGE

DEPARTMENT OF MATERIALS SCIENCE AND ENGINEERING

First-Principles Study of Photocatalytic Semiconductors using Hubbard Corrected Density Functional Theory for Hydrogen Production

WAYNE ZHAO
SPRING 2022

A thesis
submitted in partial fulfillment
of the requirements
for a baccalaureate degree
in Materials Science and Engineering
with honors in Materials Science and Engineering

Reviewed and approved* by the following:

Ismaila Dabo
Associate Professor of Materials Science and Engineering
Thesis Supervisor

R. Allen Kimel
Associate Teaching Professor of Materials Science and Engineering
Associate Head for Undergraduate Studies
Honors Adviser

*Signatures are on file in the Schreyer Honors College.

Abstract

This study focuses on the application of quantum mechanics and data-intensive methods to identify novel photocatalyst materials for use in tandem water-splitting systems. From over 130,000 inorganic materials in the Materials Project database, a list of six candidate photoanodes and three candidate photocathodes were predicted to be suitable to partake in Z-scheme water-splitting reactors. The list of 130,000 materials was pruned by removing materials having an estimated band gap outside the solar spectrum and removing materials having toxic or scarce elements, while only retaining those that have been previously synthesized and tabulated in the Crystallography Open Database. A benchmarking study on the DFT+U computational method was performed to optimize the accuracy of band gap calculations. Using these band gap predictions, six photoanodes were found to have band edges aligned with those of three photocathodes, ultimately resulting in ten theoretically viable combinations of materials for the photocatalytic splitting of water.

Table of Contents

List of Figures

List of Tables

Acknowledgements

First and foremost, I'd like to thank my family for their love and their unwavering support of my undergraduate education here in the Schreyer Honors College at Penn State.

Secondly, I am deeply grateful for my research mentor, Prof. Ismaila Dabo for his steadfast guidance on my studies and research, and my personal development as a scientist. I want to thank Nicole Hall, Quinn Campbell, and Vincent Xiong for their patient and kind mentorship on my research projects, and for teaching me invaluable computational materials science research skills in these four years I have spent in the MOSAIC (Materials Optimization and Simulation by Ab Initio Computation) group. I also thank Prof. Allen Kimel and the Department of Materials Science and Engineering at Penn State for opening doors to opportunities I would have never have been able to find otherwise.

Finally, I'd like to thank my friends for making countless fun and unforgettable memories that have kept me in good spirits throughout my time here at Penn State and even the years prior (@the townies)— and specifically thank you to those of you who kept pushing and encouraging me to persevere and finish this. . . (you know who you are).

Because of all of you, I was able to succeed and make the most out of my undergraduate time here at Penn State, and now I am able to further my education as a materials scientist by pursuing a Ph.D. degree in Materials Science and Engineering at UC Berkeley.

Chapter 1

Introduction

1.1 ABET Considerations

The development of energy-conversion technologies must not only follow scientific and technical criteria but also take into account their short- and long-term societal and environmental impacts. Following the recommendations from the Accreditation Board for Engineering and Technology (ABET), this research considers the following areas: Area 1, Economy; Area 2, Environment; Area 3, Sustainability; Area 4, Manufacturability; Area 5, Ethics; Area 6, Health and Safety; Area 7, Society; and Area 8, Policy.

The goal of this research is to discover efficient semiconductor electrodes for use in photocatalytic reactors to produce hydrogen fuels *via* water splitting, using sunlight as a renewable power source [1]. In this context, Area 1 pertains to the cost of synthesizing the photocatalysts and producing hydrogen. Area 2 relates to the selection of environmentally sustainable precursors so that toxic byproducts are not released during the synthesis or lifetime of the photocatalyst. Area 3 drives this research as its goal is to discover materials with high crustal abundance and low environmental toxicity for producing hydrogen fuels without carbon emissions. Area 4 focuses on whether the photocatalysts could be scaled industrially; it also considers whether the photocatalyst has been previously synthesized. Area 5 guides the choice of elements in the photocatalyst to be safe, relatively abundant, and ethically sourced. Area 6 addresses health and safety concerns (especially, for those working with and near the synthesized materials) while Area 7 relates to the workers and communities affected by the mining of the raw materials. Finally, Area 8 is connected to Areas 5 and 7 in that the raw materials should not be sourced from geopolitically sensitive regions and should be extracted according to international norms and best mining practices.

1.2 Climate Problem and Greenhouse Gas Emissions

Carbon dioxide (CO_2) emissions from the transportation sector alone make up nearly 30% of the total anthropogenic CO_2 emitted in the United States (US) due to a strong reliance on fossil

fuels to power the light- and heavy-duty fleets [2].

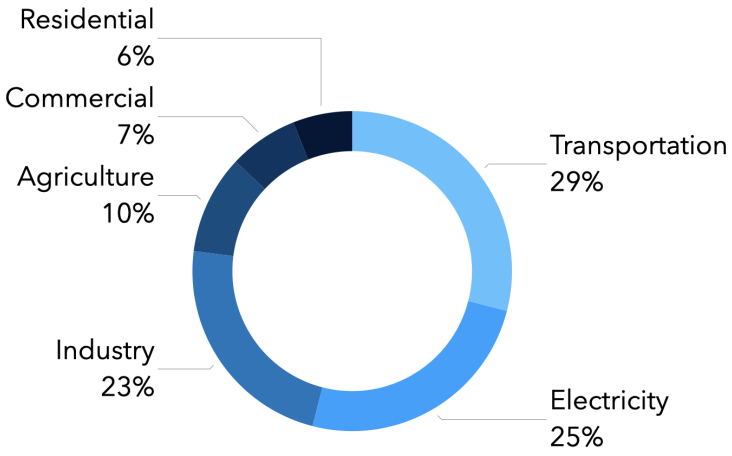

Figure 1.1: Greenhouse gas emissions in the United states by sector in 2019. This diagram shows the predominance of the transportation and industrial sectors, which together account for more than half of the total greenhouse gas emissions [2].

Hybrid and electric vehicles provide a route to gradually phase out gasoline cars and diesel trucks through the implementation of lithium-ion batteries [3]. However, larger transportation systems, such as shipping vessels, require high power and energy densities, which would result in oversized batteries (ABET Area 4) [4, 3]. Another issue with lithium pertains to its extraction (ABET Area 2); lithium mining in countries outside the US such as Chile has negatively impacted local ecosystems through soil contamination, loss of biodiversity, increased water salinity, among other adverse environmental consequences (ABET Area 2 and 8) [5]. One solution for powering the larger transportation systems is the use of compressed hydrogen gas, although the energy efficiency of this approach is limited by the energy penalty incurred during gas compression [6].

1.3 International Shipping Industry

In 2019, only 0.1% of all international shipping was powered by low-carbon technologies [7]. Large shipping vessels are primarily equipped with engines running on heavy fuel oil— an unrefined source of oil releasing sulfur compounds and other pollutant particles in addition to greenhouse gases— primarily methane and carbon dioxide [8]. International shipping demands increase

at a rate of 34% per decade leading to a pressing need to decarbonize the international shipping industry (ABET Area 1) [7, 9]. One solution proposed by Sandia National Labs is to retrofit heavy fuel oil vessels for hydrogen fuel cell vessels [4]. This study shows that the shift to hydrogen-fueled shipping vessels is both economically and technologically viable (ABET Area 2 and 4). However, hydrogen is currently sourced from steam reforming of methane into hydrogen gas, which generates carbon dioxide as main byproduct [10].

1.4 Hydrogen Fuel

Hydrogen generated from sustainable sources may serve as a clean, renewable, and dense form of energy; when used in a fuel cell, the only reaction product is water. Hydrogen can be found everywhere on Earth in the form of liquid water and has an energy density around two to three times greater by mass than those of hydrocarbon fossil fuels [11, 12]. Compared to lithium-ion batteries, hydrogen has an energy density that is potentially sixty times greater by mass [12].

However, as mentioned above, conventional methods of hydrogen production generate carbon dioxide and carbon monoxide through the steam reforming of natural gas into molecular hydrogen [10]. Therefore, clean, efficient, and cost-effective methods for the production of hydrogen should be developed and deployed.

1.5 Sustainable Hydrogen Production

Previous studies have explored the solar production of hydrogen using light and water at the surface of a semiconducting material to promote photocatalytic water-splitting [10]. The net water-splitting reaction can be written as

$$2\,H_2O \rightarrow 2\,H_2 + O_2 \tag{1.1}$$

In practical terms, this process consists of irradiating light on a photocatalytically active semiconducting material that is immersed in water. Hydrogen gas is then produced and collected [10].

For this reaction to be thermodynamically favored, the semiconducting material must fulfill specific criteria of band gap size, band edge alignment, and stability in an aqueous environment [10].

Because experimental research into photocatalysts is generally resource- and time-intensive, computational methods are of interest for screening large databases of materials and predicting their band gaps, band edge alignments, and aqueous stability at tractable computational cost before experimental characterization and testing [10]. Density-functional theory (DFT) is commonly used as an effective method for predicting band gaps. However, local and semilocal DFT approximations are known to underestimate the band gap of semiconducting materials. To address this understimation, we have benchmarked and applied a Hubbard correction method that enables for accurate and efficient predictions of band gaps [10].

1.6 Criteria for Photocatalysts

In selecting a material for overall water-splitting, one must ensure that it has a band gap large enough to perform the oxygen evolution reaction (OER) at 1.23 V (relative to the standard hydrogen electrode, SHE) and the hydrogen evolution reaction (HER) at 0 V vs. SHE. This would usually require a material with a band gap between 1.5 eV and 2.5 eV (to offer a sufficent overpotential margin) [10]. The search for photocatalytic materials that can simultaneously promote both of these reactions has been a major focus of research, but the discovery of novel materials for a tandem water-splitting system (Z-scheme) would allow for materials with band gap of less than 1.5 eV to be utilized in conjunction with a second material. Although the band gaps of both materials in a Z-scheme are smaller than 1.5 eV, one material (the photoanode) must drive the OER by aligning its valence band edge above 1.23 V vs. SHE and the other material (the photocathode) must drive the HER by aligning its conduction band edge below 0 V vs. SHE. Additionally, the conduction band of the photoanode must be below the valence band of the photocathode for electron transfer between the two photoelectrodes to be feasible, as depicted in Fig. 1.2.

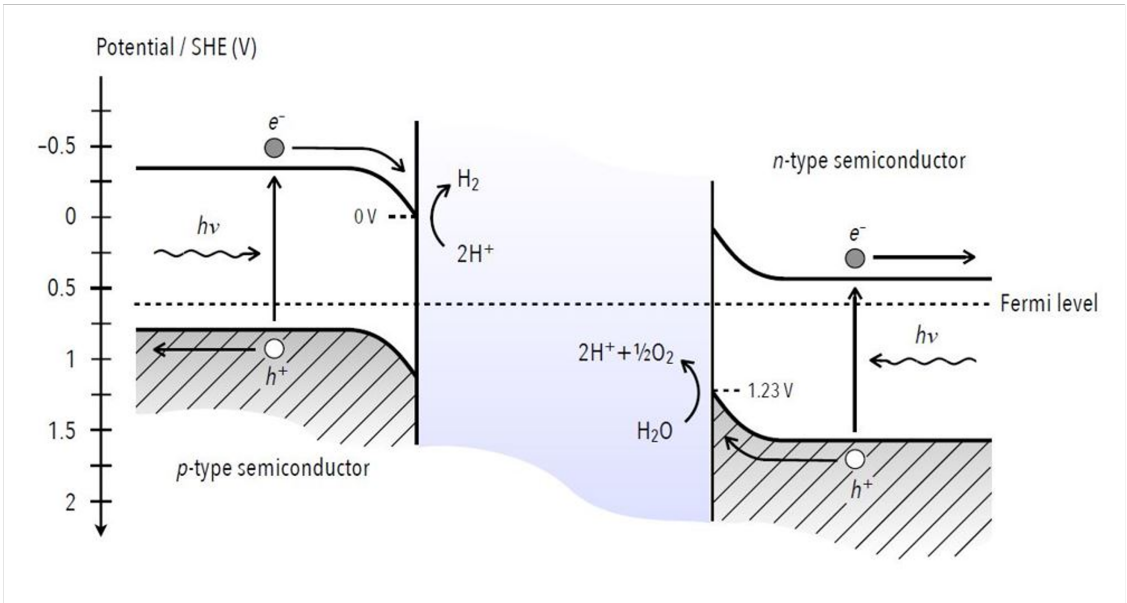

Figure 1.2: Z-scheme of a tandem photocatalytic reactor for water-splitting, showing the sequence of processes, the interfacial driving forces, and the conditions of band alignment for photocatalytic HER (left) and OER (right).

The two reactions can be coupled together using single nanoparticles, two-sided artificial 'leaf' sheet, tandem photoelectrochemical cells, tandem photocatalyst sheets, or powdered photocatalysts suspended in water [13, 14]. In order for hydrogen to compete with conventional fossil fuels, Pinaud *et al.* suggests enclosing water and small particles of both materials in a transparent polymer film [14]. This study found that a solar to hydrogen efficiency ratio of 5% may bring the production cost of hydrogen gas to \$2-4 per kg H_2 (ABET Area 1) [14]. This would allow hydrogen to be dispensed at a commercially viable price meeting the Department of Energy's target [14].

Chapter 2

Computational Methods

2.1 Many-Electron Schrödinger Equation

Overarching the theories behind quantum mechanics is the Schrödinger equation which describes the wave functions in a system. This equation can be written as

$$\hat{\mathcal{H}}\Psi(\mathbf{r}_1, \cdots, \mathbf{r}_N) = E\Psi(\mathbf{r}_1, \cdots, \mathbf{r}_N), \tag{2.1}$$

where $\hat{\mathcal{H}}$ is the many-electron Hamiltonian that captures the interactions between the atoms in a system, Ψ is the wave function that represents the eigenstates, and E represents the eigenvalues of the ground state energies of the electrons in the system.

This eigenvalue equation cannot be solved explicitly for quantum systems that have more than a few electrons because it involves multiple, coupled space variables. One approach to simplify this algorithmic complexity is density functional theory. This theory is described below.

2.2 Density Functional Theory

Density functional theory (DFT) is a computational *ab initio* modeling method for materials that starts from the bottom up — working from the mathematics and theories behind materials science — as opposed to a top-down approach — using fitted empirical data and laws for predicting a materials properties [15]. Although experiments can provide real-world empirical data, such experiments can be time and resource consuming for the study of few materials. Through the usage of supercomputers, high-throughput DFT has the ability to study numerous materials in a relatively short time-span and at relatively low cost [16].

In 1964, the physicists Walter Kohn and Pierre Hohenberg developed the idea of modeling electrons in a system as an inhomogeneous gas [15, 17]. This paved the path for applications of DFT to be used in various realms of materials science and in materials discovery [16]. DFT allows for the prediction of new materials, the optimization of their structures, and the prediction of their materials properties. One theory behind the *ab initio* aspect of DFT is the electronic structure

theory which studies the interactions between electrons and nuclei [15]. Based upon quantum mechanics, electronic structure theory uses the time-independent Schrödinger equation [15]:

$$\hat{H}\psi(\mathbf{r}) = \epsilon\psi(\mathbf{r}). \tag{2.2}$$

Using the Born-Oppenheimer approximation, the interactions between electrons and nuclei can be simplified to just the interactions of electrons due to the nuclei being orders of magnitude more massive and thus moving insignificantly compared to electrons [18]. However, solving the general form of the Schrödinger equation for materials requires other approximations provided by the Hartree-Fock equations and the Kohn-Sham equations [19]. The Hartree-Fock equations provides an approximate solution to the Schrödinger equation by estimating electron-electron interaction energy [15]. However, this approximation overestimates the exchange interaction energy [19]. This is when the Kohn-Sham equations are used by replacing the Fock exchange potential term with a local exchange potential [19]. Density functional theory solves the Kohn-Sham equations. After solving the Kohn-Sham equations to calculate the electronic band structure of a material, the electronic band gap and thus the optical band gap, can be calculated using the highest occupied and lowest unoccupied Kohn-Sham orbitals. However, DFT can underpredict the electronic band gaps by 40% compared to experimental band gaps so a Hubbard U correction value is used in the electronic band structure calculation to obtain a more accurate band gap as described in eq. 2.3 [20, 21].

$$E_{\text{DFT}+U} = E_{\text{DFT}} + E_U \tag{2.3}$$

2.3 Hubbard *U* Parameter

In a system of electrons, the exact energy with respect to the occupancy states of electrons follows a piecewise linear function with a change in slope at each empty or fully filled orbital [22, 23, 24]. Partial occupancy will follow a linear relationship between the bounds of the energy of an empty orbital and the energy of a fully filled orbital. In using DFT to estimate the energy

of a system, the deviation from the exact energy will be minimal at an empty or fully filled occupancy. However, for states near the valence band maximum or conduction band minimum, DFT underestimates the ground state energy in the system causing the energy level of the valence band maximum to be overestimated while the conduction band minimum is underestimated; this is the reasoning behind the 40% under-prediction of electronic band gaps using DFT.

Using the energy correction by the Hubbard U parameter seen in Fig. 2.1 (c). This correction in energy is zero at integer number of electrons and is a parabolic function with a maximum value at a half an electron of occupancy. Combining the energy function predicted by DFT with the energy correction provided by Hubbard U can mimic the exact energy as show in Fig. 2.1 (d) and Eq. 2.3.

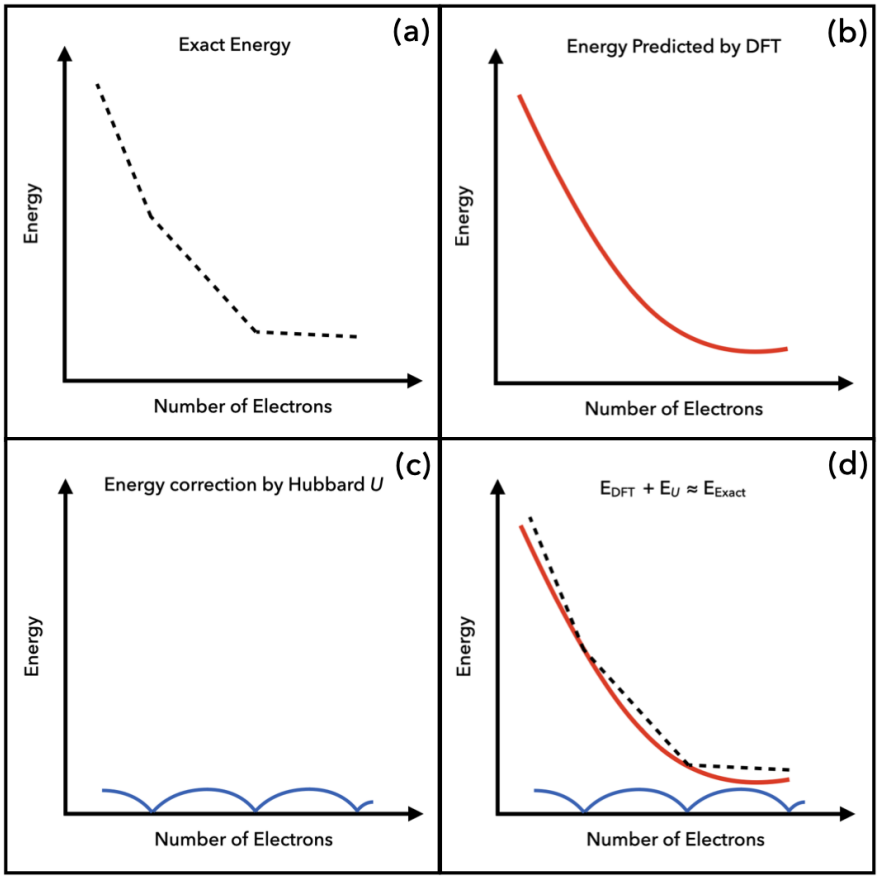

Figure 2.1: (a) shows the exact energy of an atom with respect to electron occupancy. Note that the function is a piecewise linear correlation where partial occupancy has a linear response in the change in energy of the atom [22, 23, 24]. (b) shows the energy predicted through the equations in DFT as a function of electron occupancy. (c) shows the Hubbard U correction energy as a function of occupancy. The correction energy is zero at each whole occupancy and maximum at each half electron occupancy state. (d) shows the combined functions of $E_{\text{DFT}+U} = E_{\text{DFT}} + E_U$ approximates the exact energy of an atom even at fractional occupancy states.

This study uses the Quantum Espresso software and PBE functionals in calculating DFT and DFT+U band gaps [20, 21, 25, 26, 27].

Chapter 3

Benchmarking of Computational Methods

3.1 Benchmarking Hubbard Projectors on $InGaO_3$

While running DFT+U calculations on the candidate materials, the band gap predictions, yielded unreasonably large band gap sizes in certain materials when utilizing DFT and a Hubbard correction value (+U) to all of the elements in a material. An initial benchmark test was performed on one candidate photocathode, $InGaO_3$. The application of the +U value was used to predict the band gap of $InGaO_3$ three times — applying the +U value to only one element at a time in each calculation to determine which element(s) were contributing to the unusually large band gap. The band gap values between each calculation were inconsistent; the band gap calculated using the +U value on the oxygen resulted in over twice the value of the band gaps calculated using the +U parameter applied to the indium or gallium as seen in Fig. 3.1. From there, it was concluded that the application of the Hubbard correction value to the oxygen resulted in the over-estimation of band gaps and called for a more extensive benchmarking analysis of band gap predictions with DFT+U.

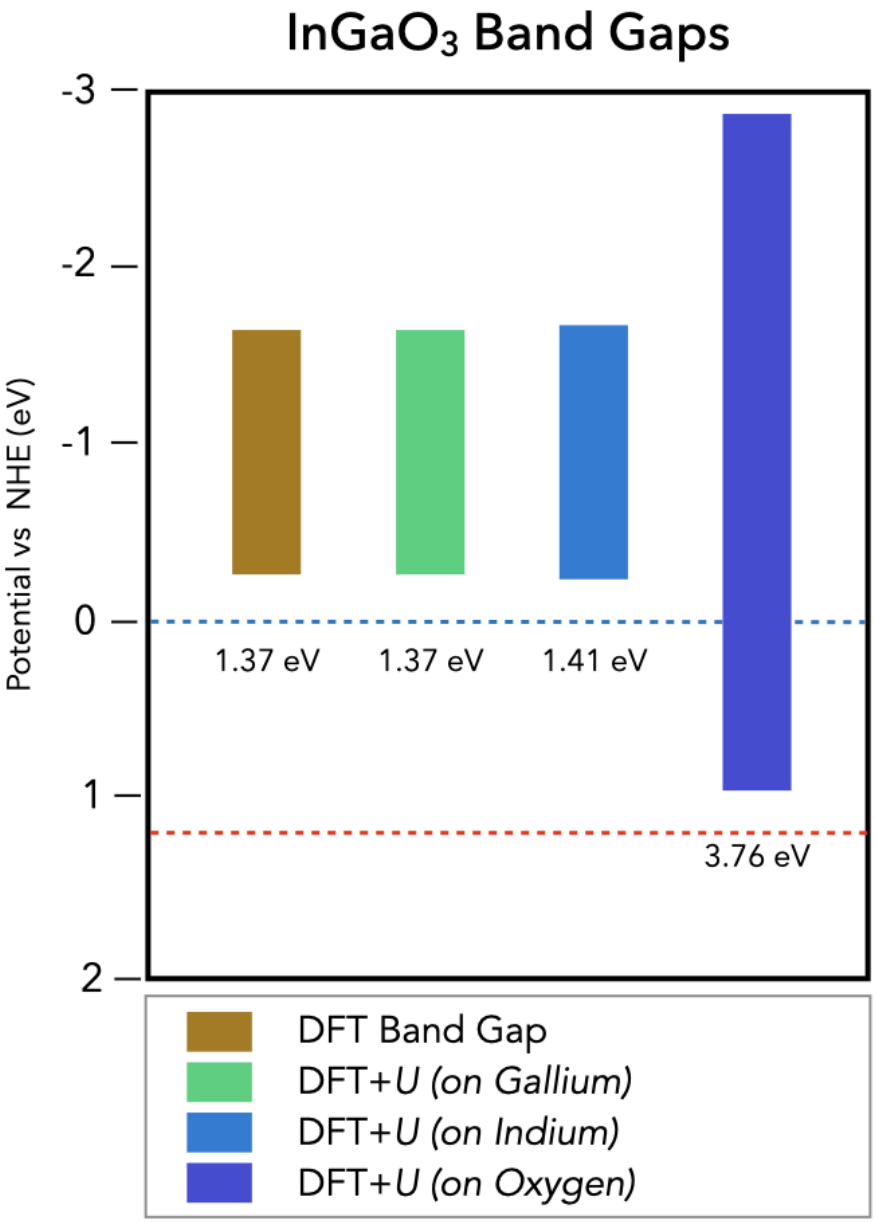

Figure 3.1: Computed $InGaO_3$ band gaps applying $+U$ on the respective element

Two calculations were then performed to determine whether using nonorthogonalized atomic orbitals or orthogonalized atomic orbitals as Hubbard projectors would yield a more accurate band gap. The Hubbard projector was only applied to the element oxygen for the same $InGaO_3$ material. From this substudy, orthogaonalized projectors were observed to calculate more accurate band gaps compared to experimentally determined band gaps. The band gap calculated from the orthogonalized Hubbard projector led to only a slight overestimation of 0.36 eV larger than the

experimentally determined band gap of $InGaO_3$ as seen in Table 3.1 [28]. From analysis of this one material, it became necessary to improve the accuracy of future band gap calculations using DFT+*U*.

Atomic Orbital Type	**DFT+*U* Band Gap**
Nonorthogonalized Hubbard Projector	7.76 eV
Orthogonalized Hubbard Projector	3.76 eV
Experimental	3.4 eV [28]

Table 3.1: Computed $InGaO_3$ band gaps versus experimentally determined band gap

3.2 Extensive Benchmarking of DFT+*U* Calculations for Predicting Band Gaps

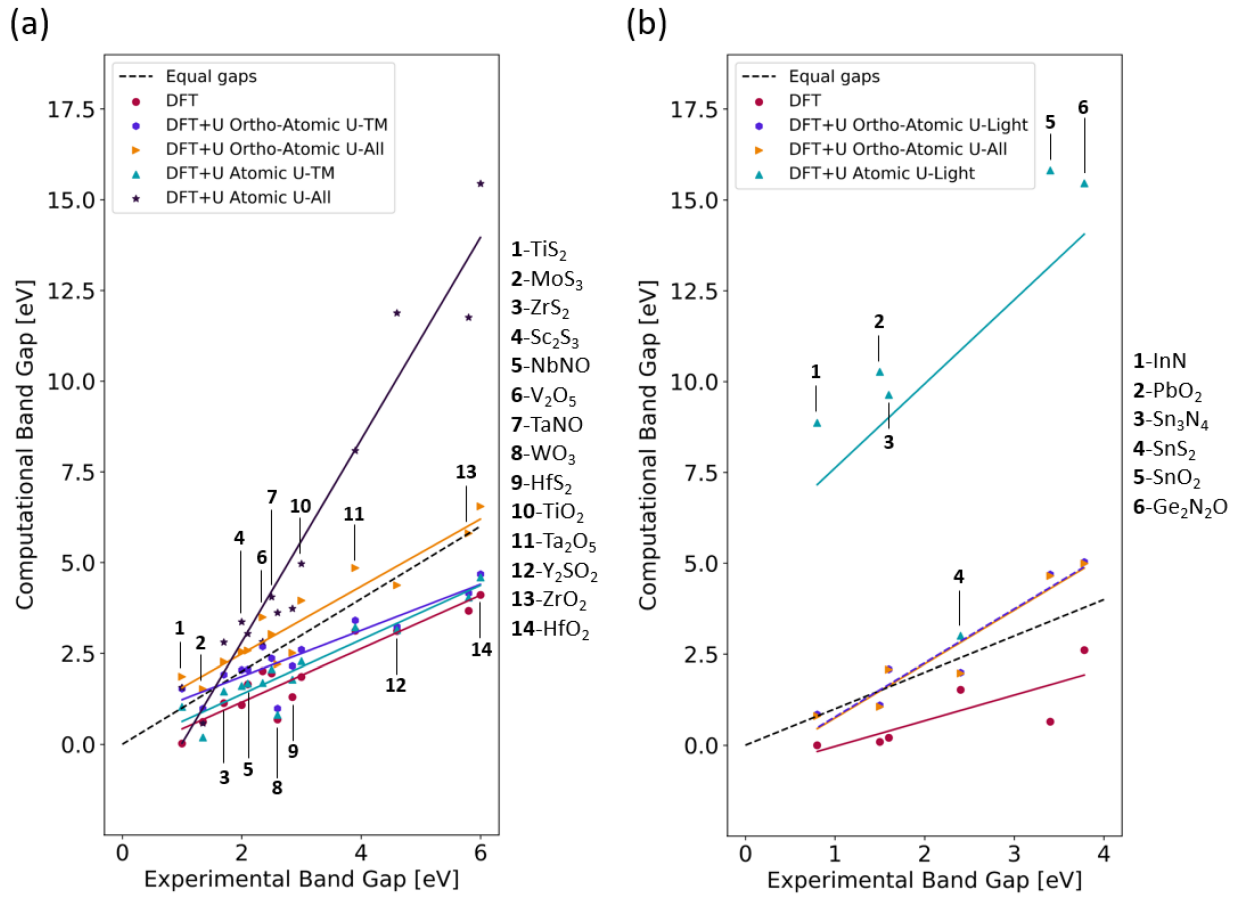

Figure 3.2: Band gaps computed with various DFT+*U* parameters and comparing to experimentally verified band gap [29].

To accurately estimate band gaps for the study of the candidate photocatalysts from the screening, an extensive benchmarking analysis of density functional theory with a correction value (DFT+*U*) was conducted using DFT+*U* calculations through the Quantum-Espresso software. This benchmark analysis performed DFT+*U* calculations on a list of twenty materials: oxides (V_2O_5, WO_3, TiO_2, Ta_2O_5, ZrO_2, HfO_2, PbO_2, and SnO_2), sulfides (TiS_2, MoS_3, ZrS_2, Sc_2S_3, HfS_2, SnS_2), nitrides (InN, Sn_3N_4), an oxysulfide (Y_2SO_2), and oxynitride materials (NbNO, TaNO, Ge_2N_2O),

and predicted their band gaps from first-principles simulations [29].

DFT was used to calculate the band gaps, but when the +U parameter was applied, the materials were split into two categories applying U to different set of elements. All 14 materials containing transition metal elements had the U parameter applied on either transition metal elements alone, or all elements in the material. Materials containing p-block (group III-IV) elements had the U parameter either applied to the light elements (N, S, and/or O) or all of the elements in the material.

3.2.1 Materials with Transition Metal Elements

For calculating the materials with transition metal elements, DFT was first used to estimate the band gap as seen in Fig. 3.2 (a). A trend line between the DFT predicted band gap and the experimentally measured band gap was created and is seen as the magenta circle points in Fig. 3.2 (a) with a magenta line for as the line of best fit. All of the DFT band gaps across the 14 materials were less than the value of the experimentally predicted band gaps.

The second calculation in benchmarking DFT+U band gap predictions was DFT+U applied to only transition metal elements while using orthogonalized projectors which are shown as the purple hexagon points with the purple trendline and labeled as "DFT+U Ortho-Atomic U-TM" in Fig. 3.2 (a). Some materials (TiS_2, ZrS_2, and V_2O_5) showed an overprediction in the size of the materials' band gap compared to experimental data. Other materials (MoS_3, WO_3, HfS_2, TiO_2, Ta_2O_5, Y_2SO_2, ZrO_2, and HfO_2 had their computationally predicted band gaps underestimate the experimental band gap, but their band gaps were all higher than the DFT predicted band gap and were thus closer to the experimental band gaps than the band gaps predicted by DFT. The remaining three materials (Sc_2S_3, NbNO, and TaNO) had accurate band gap predictions equal to their respective experimental band gap [29].

The third calculation in benchmarking DFT+U band gap predictions applied the same orthogonalized projectors with DFT+U but on both the transition elements and the light elements of N, O and S. The band gaps from these calculations are shown as the yellow triangle points with a yellow trendline and are labeled as "DFT+U Ortho-Atomic U-All" in the legend in Fig. 3.2 (a). The band gaps predicted from these calculations most closely approximated the experimental band gaps (the closeness is visually represented between the dashed black line (equal experimental to computational band gap) versus the yellow line.

The fourth and fifth sets of band gap calculations both used nonorthogonalized projectors to calculate the U parameter. The fourth calculation applied the U to only the transition metal elements and the fifth calculation applies the U to all elements — analogous to the differences between the

second and third calculation. The fourth calculation yielded results where most of the materials had band gaps two to three times larger than their experimental band gap values. These band gap sizes were similar to those calculated for $InGaO_3$ when using nonorthogonalized projectors in the band gap calculation. The fifth calculation where the U from nonorthogonalized projectors was used yielded in band gaps slightly less than the experimental values; the trendline was below the line of equal experimental vs computational band gaps. Neither of these calculation methods for materials containing transition metal elements are suitable for band gap calculations.

3.2.2 Materials with *p*-block (group III-IV) elements

Similar to the calculations for the transition metal containing materials, the *p*-block element containing materials had their band gaps calculated with DFT and three variations of DFT+U for a total of four calculated band gaps.

The DFT calculation resulted in a consistent underprediction of the band gap of the *p*-block element containing materials matching the pattern seen in the DFT band gap calculation of the transition metal containing materials.

The first variation of the U parameter used orthogonalized projectors applied to the light elements N, O and S. The second variation of the U parameter also used orthogonalized projectors but applying the U to all elements in a material. Both of these variations yielded the same band gap showing that when U is applied on *p*-block elements, the band gap size is unaffected. This can be seen in Fig. 3.2 (b) in the purple hexagon and yellow triangle points as well as their respectively colored trendlines.

Finally, the third variation uses unorthogonalized projectors to calculate the U parameter applied onto the light elements N, O and S. All six *p*-block element containing materials had band gaps many times their experimentally measured band gap which makes variation unsuitable for band gap calculations.

3.2.3 Conclusions From This Benchmarking Analysis of DFT+*U*

During the benchmarking analysis, it was found that orthogonalized projectors should be used in the calculation of the Hubbard parameter [29]. The orthogonalized projectors accounts for the Pauli-exclusion principle allowing for the band gap prediction to be more accurate when compared to experimental results. Across all twenty materials in this study, it was found that applying the Hubbard U value to the light elements (N, O, S) and transition metal elements in a material yielded the most accurate band gaps when compared to experimental literature [29]. For materials systems containing multiple metals (a mix of transition metals and or p-block elements), DFT+U applied on all elements in the material would yield the most accurate band gaps since the DFT+U would be unaffected by the presence of p-block elements and be based off the transition metal(s) and/or light non-metallic elements.

Methods from the benchmarking analysis were used in a parallel study to study band gaps of potential alkali/alkaline-earth $d10$ oxide photocatalysts. This parallel study found a balanced method of very accurate band gaps while reducing computational cost. This involves performing a single a geometry optimization, a single self consistent field calculation, the application of the Hubbard U parameter once, and a final self consistent field calculation to calculate the band gaps.

Chapter 4

Results and Discussion

4.1 Initial Screening

Of the 130,000 inorganic materials from the Materials Project database, the first step in the screening process removes materials with DFT estimated band gaps too large or too small [30]. For the photocathode, the band gap screening criteria can be seen in Fig. 4.1. The photocathode was screened such that the DFT band gap obtained from the Materials Project database must be in the range 0.4-1.5 eV and having a conduction band less than 0.2 V.

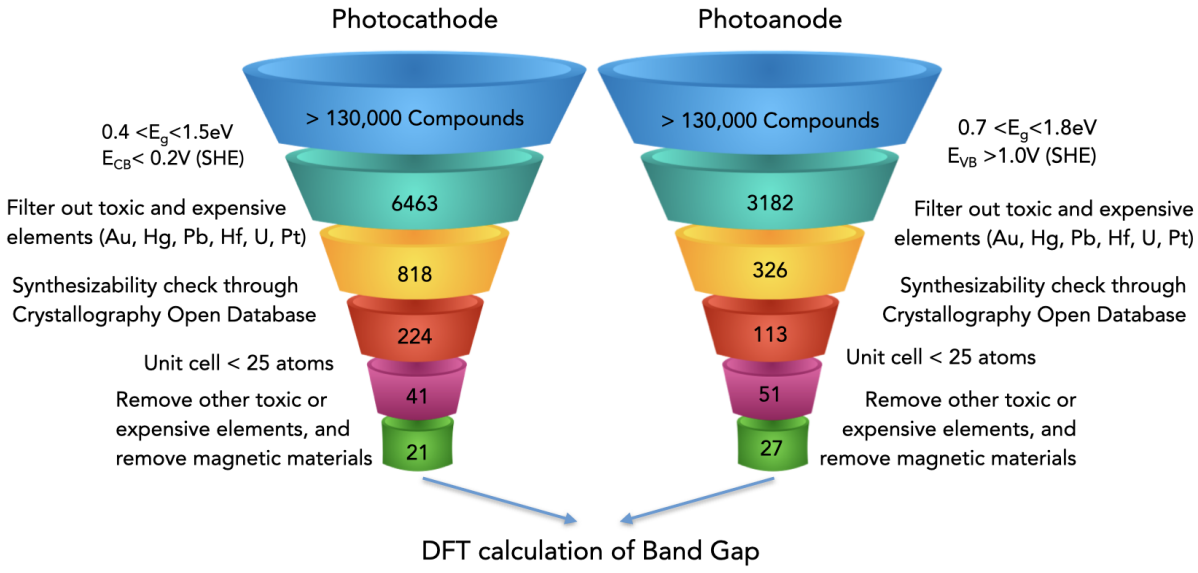

Figure 4.1: Screening Funnel used to filter down the 130,000 inorganic materials on the Materials Project database to 48 materials for DFT calculations.

This range was chosen such that when a more accurate band gap was calculated using DFT+U, the band gap would be larger and the conduction band edge would likely have an overpotential below the 0 V vs. SHE for the HER. For the photoanode, a band gap of 0.7-1.8 eV and a valence band greater than 1.0 V vs. SHE is desired for similar reasons, but needing an overpotential above 1.23 V vs. SHE for the OER. From 130,000 inorganic materials, only 6463 materials fit the band gap criteria for the photocathode and 3182 for the photoanode. In the next step, materials containing the toxic or expensive elements of Au, Hg, Pb, Hf, U, and Pt were removed leaving 818 materials for the photocathode and 326 materials for the photoanode, so cost of experimental

synthesis could be low and the process of synthesis was relatively safe (ABET Areas 1, 2, 3, 5, 6, 7). The next screening step cross-checks materials on the Crystallography Open Database to ensure the material has been experimentally synthesized (ABET Area 4) [31]. This resulted in 224 materials for the photocathode and 113 materials for the photoanode. All 224 potential photocathodes and all 113 potential photoanodes can be further studied, however, this study analyzes only the materials with a unit cell of less than 25 atoms for ease of calculation as a balance between breadth of study, accuracy, and computational cost. Counting only the materials with a unit cell of less than 25 atoms results in 41 potential photocathodes and 31 photoanodes. The aforementioned benchmarking study was then conducted and was discussed in the previous chapter; this secondary screening was then performed using methods from the benchmarking study.

4.2 Secondary Screening

After benchmarking and determining a reliable method for band gap prediction, a secondary screening process was conducted to further limit the number of materials that needed DFT+U calculation— refining the list of materials to also reduce the total computational cost, increasing yield of successful materials, and allowing for room to design safer materials.

In the secondary screening steps, more elements were added onto the screening list including As, Tc, Ru, Rh, Pd, Cd, Lu, Re, Os, Ir, Tl, Po, At, Rn, lanthanide series elements, actinide series, and elements on the last row of the periodic table. This secondary elemental screening was based upon updated information on crustal abundance and updated toxicity criteria ensuring that the synthesis process and handling of any potential photocatalysts would be safe and inexpensive to produce in the future; this would also allow for the hydrogen produced from these materials to be lower in cost (ABET Areas 1, 2, 3, 5, 6, 7) [10]. The toxicity criteria for all elements in this study must have a median lethal dosage (LD_{50}) greater than 250 mg/kg and are not radioactive. The abundance criteria for all materials in this study have a higher abundance than gold (0.004 ppm by mass). Then, using the most updated data from the Materials Project database, each of

the remaining candidate materials were then screened to remove materials with magnetic moments — removing antiferromagnetic, ferrimagnetic, and ferromagnetic materials. These materials were removed due complexities in their band gap calculations requiring greater computational resources than non-magentic materials; some of these materials could be suitable photocatalysts to be studied in the future.

DFT calculations were run through a two step process. First, a file containing atomic positions and structure of a given material was obtained from the Materials Project Database and a geometry optimization was applied to find the the most stable configuration of the atoms in the structure. Then a self consistent field (SCF) calculation was run to approximate the bandgap. This bandgap is known to be underpredicted, so materials with a DFT band gap of larger than 2 eV were filtered out. For finding the photoanode material, the material must have a band gap less than 2 eV and valence band greater than 0.575 V vs. SHE. Although this is insufficient for water splitting, the underprediction of DFT could potentially allow for the predicted DFT+U valence band edge to be above 1.23 V vs. SHE — the oxidation potential of water. Similarly for the photocathode, the band gap must be less than 2 eV and the conduction band must be less than 0.625 V vs. SHE. This resulted in 22 materials for the photoanode and 16 materials for the photocathode to further analyzed with DFT+U band gap calculations.

For DFT+U calculations, an additional two steps were completed: calculating the Hubbard parameter (+U) and a final SCF calculation. However, only materials containing an element from the following list used in the DFT+U calculation: Sc, Ti, V, Cr, Mn, Fe, Co, Ni, Cu, Zn, Y, Zr, Nb, Mo, Tc, Ru, Rh, Pd, Ag, Cd, Hf, Ta, W, Re, Os, Ir, Pt, Au, Hg, La, Ce, Pr, Nd, Pm, Sm, Eu, Gd, Tb, Dy, Ho, Er, Tm, Yb, Lu, Ac, Th, Pa, U, Np, Pu, Am, Cm, Bk, Cf, Es, Fm, Md, No, Lr, N, O, and S. Calculating the Hubbard U parameter using these elements would allow the band gap to be predicted with the greatest accuracy as recommended by the benchmark analysis [29].

After the final SCF calculation was done, the band gap and band edges were obtained from the output files by a Python script using the geometric mean of the Mulliken electronegativity (χ) of the elements in the material and the calculated band gap. The valence band edge Eq. 4.1 and the

conduction band edge Eq. 4.2 were calculated as follows:

$$E_{\text{Valence Band Edge}} = \frac{\chi_{\text{tot}}}{e} + \frac{E_{\text{g}}}{2e} \tag{4.1}$$

$$E_{\text{Conduction Band Edge}} = \frac{\chi_{\text{tot}}}{e} - \frac{E_{\text{g}}}{2e} \tag{4.2}$$

where e represents the fundamental charge of the electron, E_{g} represents the material's calculated band gap, and χ_{tot} as the geometric mean of the Mulliken electronegativity of all the elements in the material.

In total, there were twenty photoanodes and nine photocathodes for DFT+*U* to be performed. Band gaps for the materials not-containing any of the DFT+*U* elements just had their DFT predicted band gaps used for photocatalytic water splitting suitability.

4.3 Final Screening and Tandem System Formation

After DFT+*U* calculations were calculated for the twenty photoanodes and the nine photocathodes. As part of the final screening criteria, a range of band edges were chosen to find candidate photoanode and photocathode couples. The valence band edge of the photoanode must be above 1.23 V vs. SHE and the conduction band edge must be between 0-1.23 V vs. SHE for the reaction to couple with a photoanode. Likewise for the photocathode, the DFT+*U* calculated conduction band edge must be below 0 V vs. SHE, but the valence band edge must also be between 0-1.23 V vs. SHE couple with the photoanode. The scope of this study looks only at the subset of materials with DFT+*U* band gaps; materials with standard DFT estimated band gaps were excluded from this study but can be analyzed in further studies. With the two band edge criteria each for the photocathode and photoanode, only three materials were predicted to be potential photocathodes and six materials predicted to be potential photoanodes as listed in Table 4.1. This would lead to eighteen total combinations for a tandem photocatalyst device.

Table 4.1: Final list of candidate photoanode and photocathode materials that were identified using the screening criteria described in Section 4.1. Among the photoanode materials, all of the materials contained metals from the right side of the periodic table and only one contained an alkali earth metal from the left side of the periodic table. Among the photocathodes, two of the three materials contain alkali metals.

Photoanodes	**Photocathodes**
Si_2S_8	$Cs_2Ag_6S_4$
AgBr	In_4S_4
$Cu_4Te_8Br_4$	$K_2Cu_6Te_4$
$Ag_4C_2O_6$	
Cu_3TeS_3Cl	
$LiBiS_2$	

The majority of the photoanodes contain an element from the right side of the periodic table. This is likely due to the elements having a higher electronegativty than elements on the left side of the periodic table. Because the band edges are calculated using a geometric mean of the electronegativies of the elements in the material as seen in Eq. 4.2, and Eq. 4.1 the high electronegativity will shift the band edges towards 1.23 V vs. SHE OER potential. For the photocathodes, two of the three materials contain alkali metals which would likely be due to the low electronegativity of the alkali metal shifting the band edges towards the 0 V vs. SHE HER potential.

Of the eighteen total combinations, only ten combinations had systems such that the conduction band of the photoanode overlapped with the valence band of the photocathode as seen in Fig. 4.2

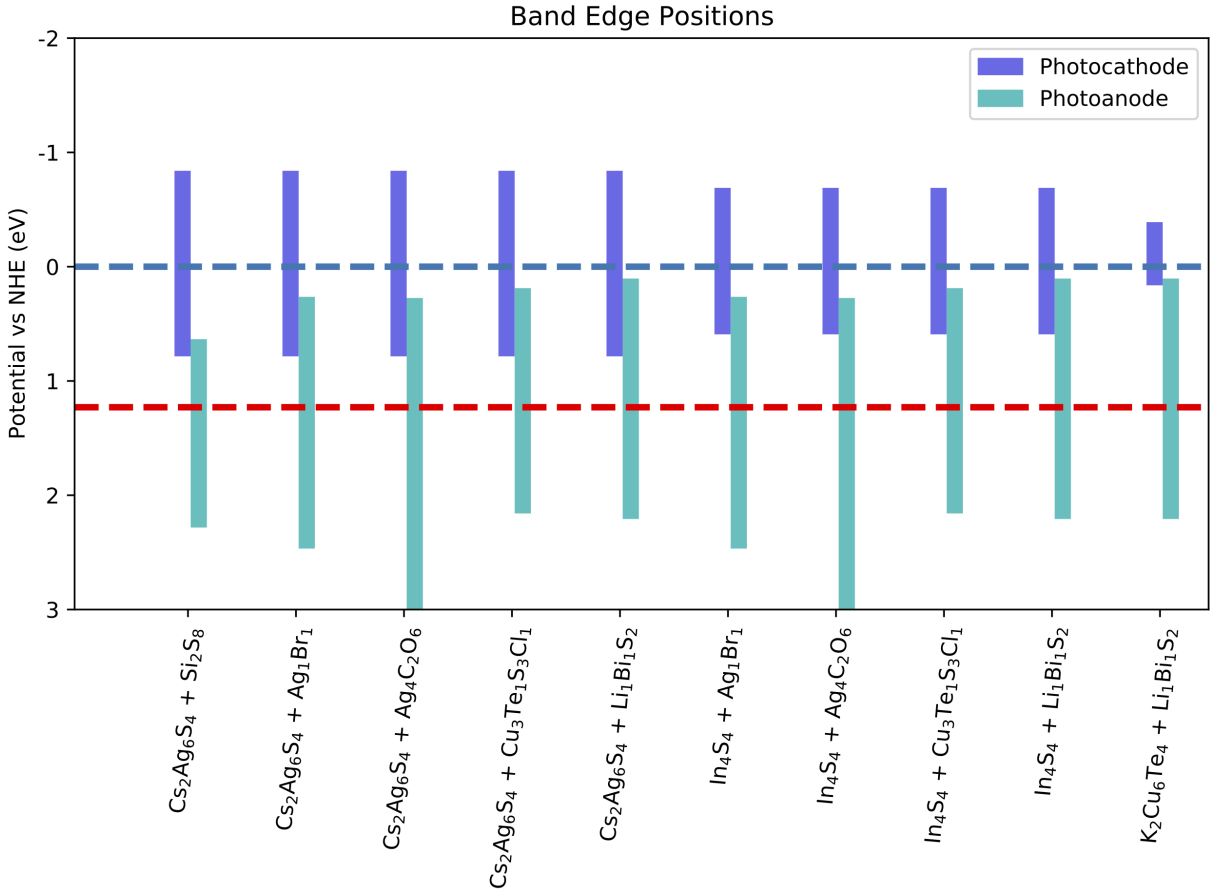

Figure 4.2: List of Viable Tandem Photocatalyst Water Splitting Systems. $Cu_4Te_8Br_4$ was the only material found to be a candidate photoanode that was unable to pair with any candidate photocathodes due to its relatively high conduction band at 0.89 V vs NHE.

Studies have suggested catalysts perform optimally at a varying range of overpotentials ranging as low as 34 mV to as high as over 570 mV [32, 33]. This could permit all ten tandem systems to have the ability to perform both the hydrogen evolution and oxygen evolution reactions.

Chapter 5

Conclusion

5.1 Conclusion

This study leveraged data from the Materials Project and employed high-throughput DFT+U calculations to determine suitability of materials for tandem photocatalytic reactors from a list of over 130,000 materials. An extensive benchmarking analysis of DFT+U was performed to optimize band gap calculations for predictive accuracy and computational efficiency [29]. A list of twenty photoanodes and nine photocathodes were analyzed using the DFT+U; from there, six materials were predicted to be suitable photoanodes while three materials were predicted to be promising photocathodes. Of the eighteen total possible combinations of tandem schemes, ten were found to have band edges correctly aligned to the HER and OER redox potentials.

5.2 Future Work

The next step in our high-throughput search is the experimental verification of the HER and OER activities of the ten proposed Z-scheme combinations. Pourbaix diagrams can be computationally generated to predict the materials' stability in water and their ability to form passivation layers against (photo)electrochemical dissolution. This study would also benefit from reconsidering the Materials Project database; since the inception of this study, several materials have been added to the database after our study while other materials entries have been updated with revised atomic positions and band gaps. In closing, stricter abundance and availability criteria should be used to ensure that all precursors can be obtained from sustainable sources without negatively impacting the global supply chains and the local communities.

Funding Statement

This research was funded by the DMREF and INFEWS programs of the National Science Foundation under Grant Agreement No. DMREF-1729338, and by the Swiss National Science Foundation (SNSF) through grant 200021-179138 and its National Centre of Competence in Research (NCCR) MARVEL.

Bibliography

[1] Nathan S Lewis and Daniel G Nocera. Powering the planet: Chemical challenges in solar energy utilization. *Proceedings of the National Academy of Sciences*, 103(43):15729–15735, 2006.

[2] United states environmental protection agency.

[3] Dong-Yeon Lee, Amgad Elgowainy, Andrew Kotz, Ram Vijayagopal, and Jason Marcinkoski. Life-cycle implications of hydrogen fuel cell electric vehicle technology for medium- and heavy-duty trucks. *Journal of Power Sources*, 393:217–229, 2018.

[4] J.W. Minnehan J.J., Pratt. Practical application limits of fuel cells and batteries for zero emission vessels. *Sandia National Lab*, 12665, 2017.

[5] Somini Sengupta. Chile writes a new constitution, confronting climate change head on somini sengupta. *New York Times*, Dec 2021.

[6] Richard Folkson. *Alternative fuels and advanced vehicle technologies for improved environmental performance: towards zero carbon transportation*. Elsevier, 2014.

[7] IEA. International shipping, Nov 2021.

[8] R. Hersher, Jul 2019.

[9] Eduardo Müller-Casseres, Oreane Y. Edelenbosch, Alexandre Szklo, Roberto Schaeffer, and Detlef P. van Vuuren. Global futures of trade impacting the challenge to decarbonize the international shipping sector. *Energy*, 237:121547, 2021.

[10] Yihuang Xiong, Quinn T. Campbell, Julian Fanghanel, Catherine K. Badding, Huaiyu Wang, Nicole E. Kirchner-Hall, Monica J. Theibault, Iurii Timrov, Jared S. Mondschein, Kriti Seth, Rebecca Katz, Andrés Molina Villarino, Betül Pamuk, Megan E. Penrod, Mohammed M. Khan, Tiffany Rivera, Nathan C. Smith, Xavier Quintana, Paul Orbe, Craig J. Fennie, Senorpe Asem-Hiablie, James L. Young, Todd G. Deutsch, Matteo Cococcioni, Venkatraman Gopalan, Héctor D. Abruña, Raymond E. Schaak, and Ismaila Dabo. Optimizing accuracy and efficacy in data-driven materials discovery for the solar production of hydrogen. *Energy Environ. Sci.*, 14:2335–2348, 2021.

[11] Norazlianie Sazali. Emerging technologies by hydrogen: A review. *International Journal of Hydrogen Energy*, 45(38):18753–18771, 2020.

[12] P.P. Edwards, V.L. Kuznetsov, W.I.F. David, and N.P. Brandon. Hydrogen and fuel cells: Towards a sustainable energy future. *Energy Policy*, 36(12):4356–4362, 2008. Foresight Sustainable Energy Management and the Built Environment Project.

[13] Boon-Junn Ng, Lutfi Kurnianditia Putri, Xin Ying Kong, Yee Wen Teh, Pooria Pasbakhsh, and Siang-Piao Chai. Z-scheme photocatalytic systems for solar water splitting. *Advanced Science*, 7(7):1903171, 2020.

[14] Blaise A. Pinaud, Jesse D. Benck, Linsey C. Seitz, Arnold J. Forman, Zhebo Chen, Todd G. Deutsch, Brian D. James, Kevin N. Baum, George N. Baum, Shane Ardo, Heli Wang, Eric Miller, and Thomas F. Jaramillo. Technical and economic feasibility of centralized facilities for solar hydrogen production via photocatalysis and photoelectrochemistry. *Energy Environ. Sci.*, 6:1983–2002, 2013.

[15] Feliciano Giustino. *Materials modelling using density functional theory*. Oxford University Press, London, England, May 2014.

[16] Juan J de Pablo, Nicholas E Jackson, Michael A Webb, Long-Qing Chen, Joel E Moore, Dane

Morgan, Ryan Jacobs, Tresa Pollock, Darrell G Schlom, Eric S Toberer, et al. New frontiers for the materials genome initiative. *npj Computational Materials*, 5(1):1–23, 2019.

[17] Pierre Hohenberg and Walter Kohn. Inhomogeneous electron gas. *Physical review*, 136(3B):B864, 1964.

[18] Max Born and Robert Oppenheimer. Zur quantentheorie der molekeln. *Annalen der physik*, 389(20):457–484, 1927.

[19] Walter Kohn and Lu Jeu Sham. Self-consistent equations including exchange and correlation effects. *Physical review*, 140(4A):A1133, 1965.

[20] Vladimir I Anisimov, Ferdi Aryasetiawan, and AI Lichtenstein. First-principles calculations of the electronic structure and spectra of strongly correlated systems: the lda+ u method. *Journal of Physics: Condensed Matter*, 9(4):767, 1997.

[21] Matteo Cococcioni and Stefano De Gironcoli. Linear response approach to the calculation of the effective interaction parameters in the lda+ u method. *Physical Review B*, 71(3):035105, 2005.

[22] John P Perdew, Robert G Parr, Mel Levy, and Jose L Balduz Jr. Density-functional theory for fractional particle number: derivative discontinuities of the energy. *Physical Review Letters*, 49(23):1691, 1982.

[23] Aron J Cohen, Paula Mori-Sánchez, and Weitao Yang. Insights into current limitations of density functional theory. *Science*, 321(5890):792–794, 2008.

[24] Aron J Cohen, Paula Mori-Sánchez, and Weitao Yang. Challenges for density functional theory. *Chemical reviews*, 112(1):289–320, 2012.

[25] John P Perdew, Kieron Burke, and Matthias Ernzerhof. Generalized gradient approximation made simple. *Physical review letters*, 77(18):3865, 1996.

[26] Paolo Giannozzi, Stefano Baroni, Nicola Bonini, Matteo Calandra, Roberto Car, Carlo Cavazzoni, Davide Ceresoli, Guido L Chiarotti, Matteo Cococcioni, Ismaila Dabo, et al. Quantum espresso: a modular and open-source software project for quantum simulations of materials. *Journal of physics: Condensed matter*, 21(39):395502, 2009.

[27] Paolo Giannozzi, Oliviero Andreussi, Thomas Brumme, Oana Bunau, M Buongiorno Nardelli, Matteo Calandra, Roberto Car, Carlo Cavazzoni, Davide Ceresoli, Matteo Cococcioni, et al. Advanced capabilities for materials modelling with quantum espresso. *Journal of physics: Condensed matter*, 29(46):465901, 2017.

[28] Tadatsugu Minami, Shinzo Takata, and Toshikazu Kakumu. New multicomponent transparent conducting oxide films for transparent electrodes of flat panel displays. *Journal of Vacuum Science & Technology A*, 14(3):1689–1693, 1996.

[29] Nicole E. Kirchner-Hall, Wayne Zhao, Yihuang Xiong, Iurii Timrov, and Ismaila Dabo. Extensive benchmarking of dft+u calculations for predicting band gaps. *Applied Sciences*, 11(5), 2021.

[30] Anubhav Jain, Shyue Ping Ong, Geoffroy Hautier, Wei Chen, William Davidson Richards, Stephen Dacek, Shreyas Cholia, Dan Gunter, David Skinner, Gerbrand Ceder, and Kristin a. Persson. The Materials Project: A materials genome approach to accelerating materials innovation. *APL Materials*, 1(1):011002, 2013.

[31] Saulius Gražulis, Daniel Chateigner, Robert T Downs, AFT Yokochi, Miguel Quirós, Luca Lutterotti, Elena Manakova, Justas Butkus, Peter Moeck, and Armel Le Bail. Crystallography open database–an open-access collection of crystal structures. *Journal of applied crystallography*, 42(4):726–729, 2009.

[32] Hoonkee Park, Ik Jae Park, Mi Gyoung Lee, Ki Chang Kwon, Seung-Pyo Hong, Do Hong Kim, Sol A Lee, Tae Hyung Lee, Changyeon Kim, Cheon Woo Moon, Dae-Yong Son, Gwan Ho Jung, Hong Seok Yang, Jea Ryung Lee, Jinwoo Lee, Nam-Gyu Park, Soo Young

Kim, Jin Young Kim, and Ho Won Jang. Water splitting exceeding 17% solar-to-hydrogen conversion efficiency using solution-processed ni-based electrocatalysts and perovskite/si tandem solar cell. *ACS Applied Materials & Interfaces*, 11(37):33835–33843, 2019. PMID: 31436403.

[33] Wei Wang, Xiaomin Xu, Wei Zhou, and Zongping Shao. Recent progress in metal-organic frameworks for applications in electrocatalytic and photocatalytic water splitting. *Advanced Science*, 4(4):1600371, 2017.

Wayne Zhao Academic Vitae

EDUCATION

PENN STATE UNIVERSITY:
BS Materials Science and Engineering
Aug. 2018 - May 2022
Schreyer Honors College
Dean's List All Semesters

TEACHING

LEARNING ASSISTANT AT PENN STATE:

INTRO TO ORGANIC CHEMISTRY (CHEM 202) | (SP 2020)

- Helped lead weekly workshops to assist students in organic chemistry outside of class. Helped answer questions in class and assisted in grading exams and worksheets.

INTRODUCTORY LABORATORY IN MATERIALS (MATSE 460) | (FA 2020, FA 2021)

- Taught X-Ray diffraction (XRD), scanning electron microscopy (SEM), energy dispersive X-ray spectroscopy (EDX)
- Taught sample preparation for powdered ceramics to make pellets for XRD, polymer and metal polishing (for optical microscopy).

GENERAL PROPERTIES LABORATORY IN MATERIALS (MATSE 462) | (SP 2021, SP 2022)

- Taught tensile strength testing of various metal and polymer samples and 4-point bend testing of ceramic Al_2O_3 samples.
- Taught differential scanning calorimetry (DSC) and dynamic mechanical analysis (DMA) of polymers and their respective sample preparation techniques.

SKILLS

PROGRAMMING:
Programming: MATLAB, Python, R, Linux commands, LaTeX

LANGUAGES:
English, Mandarin, German

SOFTWARE:
Quantum Espresso, VASP, VESTA, GMSH, Microsoft Excel, Da Vinci Resolve (Video Editor), Adobe Fresco, Canva, Adobe Spark, Adobe After Effects, Adobe Lightroom CC (Photo Editor)

RESEARCH AND PUBLICATIONS

THE MATERIALS OPTIMIZATION AND SIMULATION BY AB INITIO COMPUTATION GROUP:

Researcher | State College, PA (2018 - 2022.)

- Kirchner-Hall, N. E.; **Zhao, W**.; Xiong, Y.; Timrov, I.; Dabo, I. Extensive Benchmarking of DFT+U Calculations for Predicting Band Gaps. *Appl. Sci.* 2021, 11, 2395. DOI: 10.3390/app11052395
- Kirchner-Hall N.E.; Andrewlavage, E.; **Zhao, W**; Orbe, P.; Baksa S.; Katz, R.; Kahn M.; Xiong, Y.; Campbell, Q. T. Schaak R.; Dabo, I. Data-Driven Discovery of Alkali/Alkaline-Earth p-block Oxides for Photocatalytic Water Splitting
- DOSpkg for DFT and DFT+U with Quantum-Espresso Implemented a software package that automates projected density of states calculations for compounds in the Materials Project database. github.com/wuz75/DOSpkg
- High-Throughput Search for Water Splitting Photocathodes and Photoanodes

LONG-QING CHEN RESEARCH GROUP:

Researcher | State College, PA (2019)

- Electronic-Structure Calculation of Surface Energy for Perovskite Materials
- Applied the Vienna Ab-initio Simulation Package (VASP) to perform DFT calculations to calculate surface energies of perovskite materials. Constructed supercells of perovskites using the Visualization for Electronic Structural Analysis (VESTA) software. Presented poster at the Research Symposium of the NASA PA Space Grant Consortium Research Internship Program

EXTRACURRICULAR ACTIVITIES

PENN STATE GLEE CLUB
Baritone | (2022)

PENN STATE PHILHARMONIC ORCHESTRA
Violin | (2022)

PENN STATE CAMPUS ORCHESTRA
Violin | (2019 - 2021)

- Concertmaster (2020-2021)
- Associate Concertmaster (2019)